

Strongly correlated double Dirac fermions

Domenico Di Sante,¹ Andreas Hausoel,¹ Paolo Barone,² Jan M. Tomczak,³ Giorgio Sangiovanni,¹ and Ronny Thomale¹

¹*Institut für Theoretische Physik und Astrophysik, Universität Würzburg, Am Hubland Campus Süd, Würzburg 97074, Germany*

²*Consiglio Nazionale delle Ricerche (CNR-SPIN), Via Vetoio, LAquila, Italy*

³*Institute of Solid State Physics, Vienna University of Technology, A-1040 Vienna, Austria*

(Dated: March 30, 2017)

Double Dirac fermions have recently been identified as possible quasiparticles hosted by three-dimensional crystals with particular non-symmorphic point group symmetries. Applying a combined approach of ab initio methods and dynamical mean field theory, we investigate how interactions and double Dirac band topology conspire to form the electronic quantum state of Bi_2CuO_4 . We derive a downfolded eight-band model of the pristine material at low energies around the Fermi level. By tuning the model parameters from the free band structure to the realistic strongly correlated regime, we find a persistence of the double Dirac dispersion until its constituting time reversal symmetry is broken due to the onset of magnetic ordering at the Mott transition. We analyze pressure as a promising route to realize a double-Dirac metal in Bi_2CuO_4 .

Introduction. Electrons in solids witness a reduced spatial symmetry in comparison to the spacetime continuum. While the high-energy perspective constrains us to Majorana, Weyl, and Dirac fermions in accordance with the inhomogeneous Lorentz (or Poincaré) group, electronic quasiparticles in solids at low energies can display emergent fermionic behaviour within and even beyond this classification [1, 2]. Graphene constitutes one of the most prominent material discoveries where Dirac-type quasiparticles have been realized [3]. The current rise of Weyl semimetals [4], along with Majorana quasiparticles in superconducting heterostructures [5, 6], complements this evolution in contemporary condensed matter physics.

Recently, Wieder *et al.* [1] have brought up the possibility to realize double Dirac quasiparticles in certain 3D crystals with specific non-symmorphic point group symmetry. This was followed up on by a systematic analysis of all double space groups (SGs) accounting for $S = 1/2$ electrons in spin-orbit coupled crystals with time reversal symmetry [2]. In particular, SG 130 and 135 were found to establish eminently suited ground for generic double Dirac fermions protected by point group symmetry. Among all material candidates for SG 130, it is already realized in Ref. 2 that Bi_2CuO_4 might be a prime candidate due to its filling-enforced semimetallicity [7], nurturing the hope to observe double Dirac fermions close to the Fermi level. All such band structure classifications, however, always need to be extended to account for the role of interactions in the material, which turn out to be of vital relevance in Bi_2CuO_4 . Most of the topological band properties, even the metallic ones, display a certain degree of persistence against weak interactions as long as those do not break any protecting symmetry. Interaction-induced instabilities, however, do change the symmetry class of the quantum state, possibly affecting the whole range of constituting symmetries including charge conservation, time reversal, and point group operations.

In this Letter, we study strong interaction effects of double Dirac fermions, analyzing the band structure properties and correlation effects in Bi_2CuO_4 . From density functional theory, we distill an effective eight-band tight-binding Hubbard model which is dominated by the $d_{x^2-y^2}$ orbital of the four Cu atoms in the unit cell. Spin-orbit coupling (SOC) is found to be weak because the heavy atoms of the compound do not significantly contribute to the low-energy density of states. As expected, the double Dirac dispersion is located close to the Fermi energy, as identified by an 8-fold band degeneracy at the A point. We quantify the strength of electron-electron interactions by means of the constrained random phase approximation (cRPA). By employing a combined approach of density functional theory (DFT) and dynamical mean field theory (DMFT), we determine the critical value for the Mott transition at ambient pressure to be $U_{\text{Mott}} \approx 0.85\text{eV}$. This value is approximately equal to the $d_{x^2-y^2}$ bandwidth, and substantially smaller than $U_{\text{cRPA}} \approx 1.58\text{eV}$, suggesting that Bi_2CuO_4 at ambient pressure parametrically locates itself deep in the Heisenberg limit of the Mott regime. Below the Néel temperature T_N the magnetic state displays an AFM-C type collinear order of the four local Cu magnetic moments. In the stoichiometric compound at pristine conditions, magnetism thus dominates the electronic state, rendering the double Dirac fermions inaccessible. We explore the effect of hydrostatic pressure to drive Bi_2CuO_4 into a metallic phase where the double Dirac fermions emerge. We find the bandstructure formation and correlation effects of Bi_2CuO_4 to be highly sensitive to pressure. Starting from ambient pressure, we find an initial change of the magnetic ordering from AFM-C to AFM-G type, along with a reduced on-site Coulomb repulsion. This could pave the way towards a high-pressure double Dirac metal.

Band structure and effective tight-binding model. Bi_2CuO_4 crystallizes in the tetragonal space group

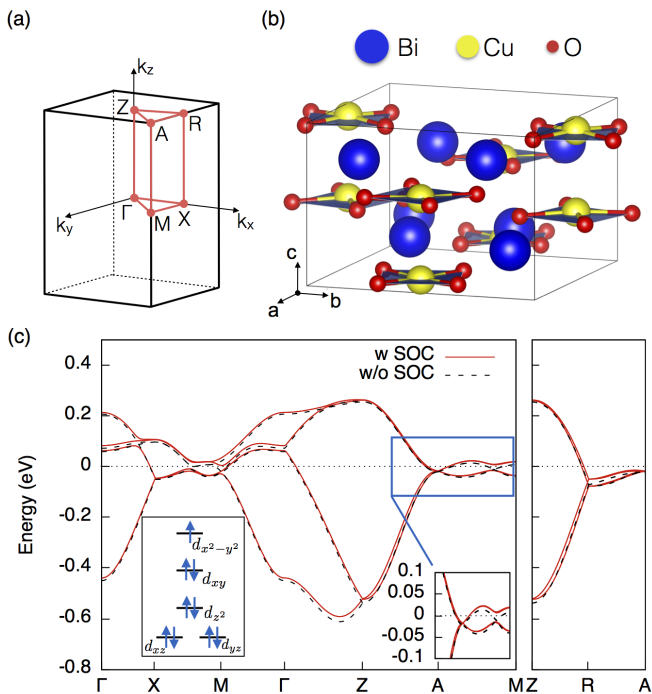


FIG. 1: (Color online) (a) Tetragonal Brillouin zone of SG 130 P4/ncc with corresponding high-symmetry points. (b) Crystal structure of Bi_2CuO_4 . Atom colors: Bi = blue, Cu = yellow, O = red. Blue plaquettes highlight the square-planar CuO_4 coordination. (c) DFT bandstructure in the metallic phase with (red solid line) and without (black dashed line) SOC. The left inset is a schematic representation of the square-planar crystal field and orbital filling for Cu-type d^9 . The right inset shows a zoom around the eight-fold degenerate A point, which comes along a characteristic four-fold degeneracy along the R-Z line.

TABLE I: Hopping integrals in meV between the $d_{x^2-y^2}$ -type Wannier functions on different Cu atoms for different pressure P [GPa] with ambient pressure $P = 0$ GPa. The first row takes over the notation introduced in Ref. [8], while $t_{i,j}$ in the second row is transfer integral between Cu- i and Cu- j site ($i, j = 1..4$) as in Fig. 2. When a j index has a superscript ± 1 it refers to a Cu- j atom in the $[00\pm 1]$ unit cell. U_{cRPA} (eV) is the cRPA value for the effective onsite Coulomb interaction. The $P = 0$ hopping values in parenthesis refer to Ref. [8].

P	t_{1u}^{AB}	t_{1d}^{AB}	t_{2u}^{AB}	t_{2d}^{AB}	t_1^A	t_2^A	U_{cRPA}
	$t_{1,2}$	$t_{4,2}$	$t_{1,3}$	$t_{1,2-1}$	$t_{1,4}$	$t_{1,1^1}$	
0	66	40	5	-24	36	-20	1.58
	(74)	(36)	-	(-40)	(21)	(-18)	
30	80	21	6	-20	73	-16	1.45
50	88	13	2	-13	65	-7	1.36

P4/ncc (SG 130) (Fig. 1(a)) [9]. Four inequivalent Cu atoms in the unit cell share a square-planar CuO_4 coordination, stacked along the out-of-plane direction and intercalated by Bi atoms, as depicted in Fig. 1(b). The Cu-O hybridization is quite strong, leading to a

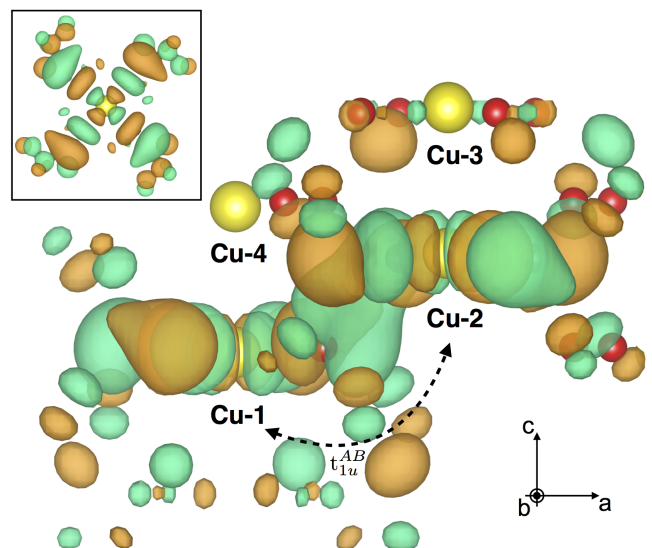


FIG. 2: (Color online) Side view of the $d_{x^2-y^2}$ -type MLWFs belonging to two neighbouring Cu-chains, responsible for the transfer integral t_{1u}^{AB} (Tab. I). Brown (green) color refers to positive (negative) values of the MLWF. The individual MLWFs are not symmetric with respect to the CuO_4 plaquette plane. This is due to a small off-centering of the Cu atoms, in opposite directions for Cu-1 and Cu-2. The inset shows a top view on the Cu-1 $d_{x^2-y^2}$ -type MLWF.

mixed d - p character of the band structure of the occupied states [10]. The Bi- p manifold only starts ≈ 1.5 eV above the Fermi level, suggesting that the low energy model is given by Cu and O electronic states. The square-planar crystal field is characterized by a higher-in-energy $d_{x^2-y^2}$ orbital experiencing a head-to-head interaction with the O- p . The level separation is schematically drawn in the left inset of Fig. 1(c). Cu is nominally in the oxidation state 2+ (i.e. d^9 configuration). For this reason, a half-filled $d_{x^2-y^2}$ -derived single spin-degenerate band per Cu atom in the unit cell is expected to dominate at low energies. Fig. 1(c) displays the band dispersion of the electronic states around the Fermi level. Due to the dominant Cu orbital, the effect of SOC is almost negligible, only inducing small spin splittings. We estimate the energy scale of SOC to be ≈ 20 meV. Despite its small scale, however, SOC is a crucial ingredient for the symmetries in the double SG representation that ensure the existence of a double Dirac fermion with linear dispersion at the Brillouin zone corner $A = (\pi, \pi, \pi)$. As the band filling is given by an odd multiple of 4 ($180 = 8 \times 22 + 4$), the double Dirac fermion in Bi_2CuO_4 is located almost at the Fermi level, as visible in the right inset of Fig. 1(c).

While the aforementioned electronic structure details, as well as the magnetic properties at ambient pressure, have already been analyzed previously [8, 11], a closer inspection of the hybridization profile and the Coulomb matrix elements in terms of ab-initio derived maximally

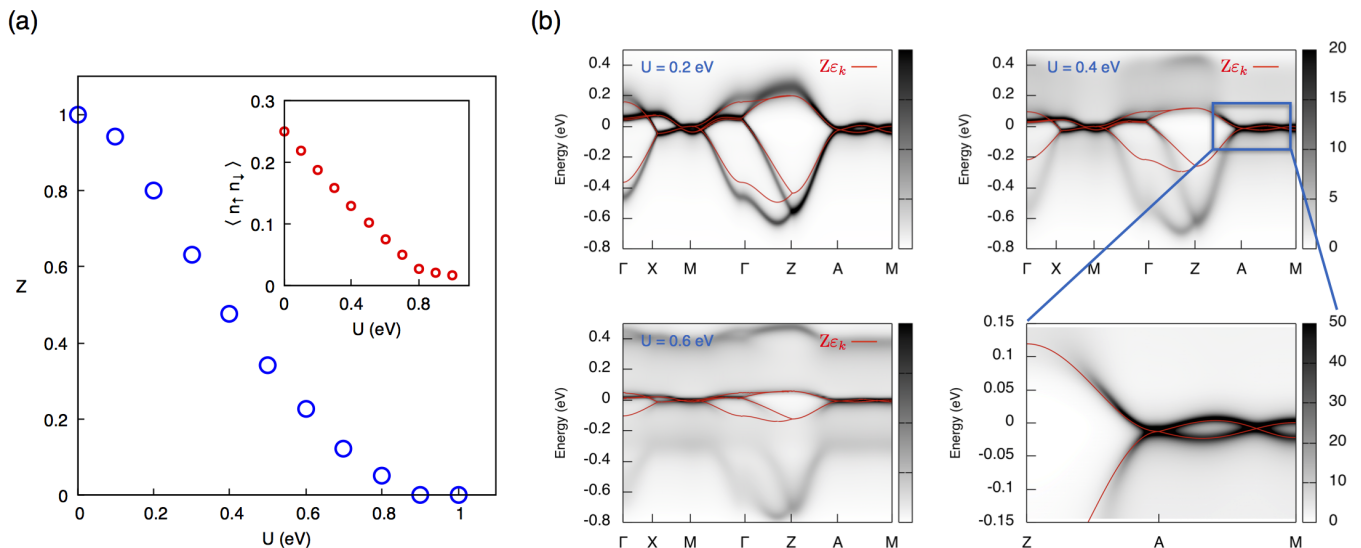


FIG. 3: (Color online) (a) DMFT quasiparticle weight Z (main panel) and double occupancies (inset) as a function of U in the paramagnetic phase for a temperature $\beta = 100$ eV $^{-1}$. The Mott transition occurs at $U_{\text{Mott}} \approx 0.85$ eV. (b) Momentum-resolved DMFT spectral function $A(k, \omega)$ for $U = 0.2, 0.4$, and 0.6 eV. Red lines denote the DFT band structure renormalized by the DMFT quasiparticle weight Z . For $U = 0.4$ eV, the zoom shows the preservation of the eight-fold degenerate A point along with an already significant band renormalization.

localized Wannier functions (MLWFs) [12] is indispensable to further analyze the fate of double Dirac fermions in the presence of interactions. The relatively large extension of the MLWFs is a consequence of the strong Cu-O hybridization. Their lobes indeed stretch out over the O-atoms with a clockwise winding shape, as shown in the top view of Fig. 2. Our analysis elucidates the origin of the strong three-dimensional character of Bi₂CuO₄, as the MLWFs extend along the out-of-plane direction in an asymmetric manner, which is a consequence of buckled CuO₄ plaquettes. Moreover, two $d_{x^2-y^2}$ -type MLWFs localized on different chains have a strong overlap, even though they do not belong to the same ab -plane. This is illustrated by the t_{1u}^{AB} transfer integral shown in Fig. 2 and Tab. I. Coherent electron hopping is also enabled between neighbouring plaquettes along the normal c -direction. This process is accounted for by the transfer integral t_1^A , which is indeed comparable with the hoppings t_{1u}^{AB} and t_{1d}^{AB} that involve a significant in-plane component. As further discussed below, the hoppings turn out to be rather sensitive to pressure, and even impose a change of the magnetic ordering pattern, which is relevant to classifying the possible topological character of symmetry-broken phases in Bi₂CuO₄ [13].

Mott transition and spectral function. Having obtained an effective band structure description of Bi₂CuO₄ close to E_F in terms of a half-filled single band per Cu atom, we focus on the double Dirac point at the A point. In particular, we analyze its evolution as a function of interaction strength, starting from the free electron limit up to the realistic cRPA value for the electron-electron inter-

action U [14]. Bi₂CuO₄ is parametrically located within the applicability bounds of DFT+DMFT, partly because of its three-dimensional character. Fig. 3(a) displays the quasiparticle weight $Z = (1 - \partial \text{Im} \Sigma(\omega) / \partial \omega|_{\omega \rightarrow 0})^{-1}$. Before reaching U_{CRPA} , we encounter a Mott-type metal-to-insulator transition (MIT) at $U_{\text{Mott}} \approx 0.85$ eV. At the Mott transition, the quasiparticle weight is suppressed by interactions, and the fraction of doubly-occupied Cu-sites $\langle n_{\uparrow} n_{\downarrow} \rangle$ reduces from the free-particle value of 1/4 towards zero (inset in Fig. 3(a)). At intermediate U , the spectral function, as depicted in Fig. 3(b), is well described by the DFT single particle band structure renormalized in terms of bandwidth by the quasiparticle weight Z , along with the appearance of incoherent lower and upper Hubbard bands. Since the double Dirac fermion is located close to the Fermi level, it contributes to the quasiparticle peak for interaction strengths below the Mott transition. Even though the double Dirac velocities are strongly reduced by electron-electron interactions, the eightfold-degeneracy of the double Dirac point is preserved up to U_{Mott} . Within DMFT, as long as we consider the paramagnetic phase which does not allow the system to undergo a magnetic phase transition, the double Dirac point does not get destroyed for larger U . Yet, its weight gets damped by electron-electron scattering, and transferred towards the high-energy (Hubbard) bands, alongside with the whole low-energy spectral weight.

Magnetic order and hydrostatic pressure. At U_{CRPA} , allowing for magnetic ordering, the DFT+DMFT ground state of Bi₂CuO₄ is not paramagnetic, but displays intra unit cell magnetic order. As a consequence, the double

TABLE II: DFT+U total energy differences (meV/unit cell) for the magnetic patterns at ambient pressure and at 30 GPa. The lowest-lying AFM type state is chosen as reference energy. Non-magnetic (NM) and ferromagnetic (FM) configurations are higher up in energy than the AFM states.

P (GPa)	U (eV)	NM	FM	AFM-C	AFM-G	AFM-A
0	0.0	442	88	0	2.4	54
	0.5	555	77	0	2.2	49
	1.58	812	60	0	1.8	41
	2.1	940	54	0	1.6	37
30	1.45	636	97	28	0	65

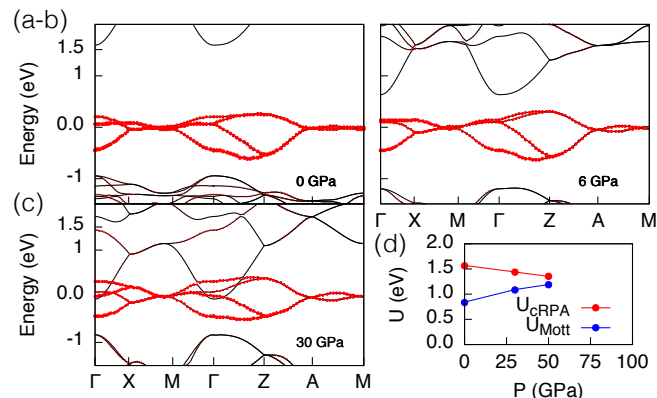


FIG. 4: (Color online) (a-c) Evolution of the DFT band structure for $P = 0$ (ambient pressure), 6, and 30 GPa. Red symbols refer to the $d_{x^2-y^2}$ character. (d) U_{cRPA} and U_{Mott} as a function of pressure. It is suggestive to expect an insulator to metal transition around $P = 50 - 60$ GPa.

Dirac cone is absent due to the breaking of time-reversal symmetry. This finding holds for finite temperature T , below the Néel temperature T_N . For $T > T_N$, while there is no long-range magnetic order, the broadening is too strong to resolve detailed dispersive features. In Tab. II, we report the DFT+U energies at $T = 0$ for different magnetic configurations. Mapping these energies on a Heisenberg model and performing classical Monte Carlo simulations, we estimate a Néel temperature of 56 K for $U = 1.58$ eV, which compares reasonably well with the experimental value of 50 K [8–10]. The AFM-C type configuration, characterized by a ferromagnetic alignment of the chains along the c -direction, is found to be preferred. Independent of the considered interaction strength, however, it is always energetically close to an AFM-G type phase, where the magnetic moments are antiferromagnetically aligned along all three directions. This is the consequence of a competitive balance between t_1^A and t_{1d}^{AB} transfer integrals (Tab. I). This tuned frustration is relieved by pressure, favoring t_1^A over t_{1d}^{AB} . It explains why we observe a change to AFM-G type magnetic order

as a function of pressure (see Tab. II).

Along with the change of the magnetic order, pressure has a profound impact on the electronic structure. As illustrated in Fig. 4(a-c), the bands above and below the $d_{x^2-y^2}$ manifold get closer to the Fermi level. This results in a more efficient screening of the Coulomb interaction for the target $d_{x^2-y^2}$ states. Fig. 4(d) and TABLE I report the corresponding reduction of U_{cRPA} . In addition, the slight increase of the $d_{x^2-y^2}$ bandwidth ($\sim 10\%$) leads to a larger critical U_{Mott} for the Mott transition. Even though U_{cRPA} remains larger than U_{Mott} all the way up to 50 GPa [15], the trend towards the restoration of the metallic phase is evident [16]. Assuming the absence of a structural phase transition [15], this suggests a transition into a high-pressure double Dirac metal for $\simeq 60$ GPa.

Conclusion. Our analysis identifies Bi_2CuO_4 as a prototypical material where crystal structure and orbital character conspire to give rise to correlated double Dirac fermions close to the Fermi level. At ambient pressure, the interactions turn out to drive the system into Mott state along with magnetic intra-cell ordering where the double Dirac cone is absent. As a function of hydrostatic pressure, we find that the material could be driven into a metallic state where the double Dirac features would emerge. For this, our ab initio calculations indicate a pressure regime of ≈ 60 GPa, which is still within the range of experimental pressure cell transport setups. Our study suggests several routes to realize a double-Dirac metal in Bi_2CuO_4 at low temperatures. For instance, a combined pressure and doping approach could establish a convenient perturbation of the pristine material in order to render correlated double Dirac fermions accessible to experimental investigation.

We are grateful to B. A. Bernevig for drawing our attention to double Dirac fermions, and to C. Felser for detailed information on Bi_2CuO_4 crystals. We thank M. Baldini, J. Cano, A. Schnyder, and A. Toschi for helpful discussions. This work was supported by DFG-SFB 1170 Tocotronics, ERC-StG-336012-Thomale-TOPOLECTRICS, and NSF PHY-1125915. The authors acknowledge computational resources from the Leibniz Supercomputing Centre under the Project-ID pr94vu.

- [1] B. J. Wieder, Y. Kim, A. M. Rappe, and C. L. Kane, Phys. Rev. Lett. **116**, 186402 (2016).
- [2] B. Bradlyn, J. Cano, Z. Wang, M. G. Vergniory, C. Felser, R. J. Cava, and B. A. Bernevig, Science **353**, 558 (2016).
- [3] A. H. Castro Neto, F. Guinea, N. M. R. Peres, K. S. Novoselov, and A. K. Geim, Rev. Mod. Phys. **81**, 109 (2009).
- [4] X. Wan, A. M. Turner, A. Vishwanath, and S. Y. Savrasov, Phys. Rev. B **83**, 205101 (2011).
- [5] N. Read and D. Green, Phys. Rev. B **61**, 10267 (2000).

- [6] L. Fu and C. L. Kane, *Phys. Rev. Lett.* **100**, 096407 (2008).
- [7] H. C. Po, H. Watanabe, M. P. Zaletel, and A. Vishwanath, *Science Advances* **2**, e1501782 (2016).
- [8] O. Janson, R. O. Kuzian, S.-L. Drechsler, and H. Rosner, *Phys. Rev. B* **76**, 115119 (2007).
- [9] J. L. Garcia-Munoz, J. Rodriguez-Carvajal, F. Sapina, M. J. Sanchis, R. Ibanez, and D. Beltran-Porter, *Journal of Physics: Condensed Matter* **2**, 2205 (1990).
- [10] See Supplemental Material at <http://xxxx.xxxx>.
- [11] A. Goldoni, U. del Pennino, F. Parmigiani, L. Sangaletti, and A. Revcolevschi, *Phys. Rev. B* **50**, 10435 (1994).
- [12] N. Marzari, A. A. Mostofi, J. R. Yates, I. Souza, and D. Vanderbilt, *Rev. Mod. Phys.* **84**, 1419 (2012).
- [13] A. Schnyder, private communication.
- [14] The value for U_{cRPA} is defined as the local minus the nearest-neighbor part of the cRPA Coulomb matrix element as shown in Tab. I.
- [15] So far, pressure effects have been hardly investigated in Bi_2CuO_4 . In [17], the occurrence of a structural phase transition might have been observed within 20 GPa and 37 GPa, but demands further analysis.
- [16] The most reliable feature is the trend observed as a function of pressure rather than the absolute values of the Coulomb interaction strength obtained through cRPA. The absolute accuracy of cRPA is challenged by (i) the slight tendency to underestimate the Coulomb matrix elements, (ii) the mapping of the non-local cRPA Coulomb interaction onto a local Hubbard model, and (iii) the absence of all non-local correlations within the DMFT approximation. The latter is known to reduce the Néel temperature of about 30-40% in 3D systems [18].
- [17] F. X. Zhang, B. Manoun, S. K. Saxena, and C. S. Zha, *J. Solid State Chem.* **179**, 1202 (2006).
- [18] G. Rohringer, A. Toschi, A. Katanin, and K. Held, *Phys. Rev. Lett.* **107**, 256402 (2011).

DFT+DMFT COMPUTATIONAL DETAILS

Density functional theory calculations were performed by using the VASP ab-initio simulation package [1] within the projector-augmented-plane-wave (PAW) method [2, 3]. The generalized gradient approximation as parametrized by the PBE GGA functional for the exchange-correlation potential was used [4], by expanding the Kohn-Sham wavefunctions into plane-waves up to an energy cut-off of 600 eV. The Brillouin zone has been sampled on a $8 \times 8 \times 12$ regular mesh, and when considered, spin-orbit coupling (SOC) was self-consistently included [5]. The low energy model has been extracted by projecting onto Cu $d_{x^2-y^2}$ -like maximally localized Wannier functions (MLWF) using the WANNIER90 package [6]. Electron-electron interaction was included within the framework of dynamical mean field theory (DMFT), by mapping the lattice problem into an impurity model subject to a self-consistency condition [7]. We solved the impurity model by continuous-time quantum Monte Carlo, as implemented in the w2dynamics package [8, 9].

SETTING UP THE $d_{x^2-y^2}$ LOW-ENERGY HAMILTONIAN

Ab initio computation of the screened Coulomb interaction

Our aim is to set up a Hamiltonian that faithfully represents the low-energy electronic degrees of freedom of our material. In particular, we need to compute the strength of the Coulomb repulsion experienced by charge carriers that reside in states close to the Fermi level. In a solid, the polarizability of charges screens the bare Coulomb repulsion $v(\mathbf{r}, \mathbf{r}') = \frac{e^2}{4\pi\epsilon_0} 1/|\mathbf{r} - \mathbf{r}'|$. When setting up a Hamiltonian for low-energy excitations, its Coulomb interaction thus needs to be screened by all excitations that are not included in that Hamiltonian.

A successful approach to disentangle and determine screening effects for the Coulomb interaction is the constrained random phase approximation (cRPA)[10]. To be on par with the many-body Hamiltonian used in the main manuscript, we here (i) include all contributions to the charge polarization except for those that are confined (constrained) to the subspace of Cu- $d_{x^2-y^2}$ bands that constitute the low-energy spectrum, and (ii) express the partially screened Coulomb interaction in a basis of maximally localized Wannier functions[11].

The underlying DFT calculations employ a full potential LMTO method [12], a Brillouin zone discretized into $8 \times 8 \times 8$ k -points, local orbitals for the Bi-5d states, and neglects the spin-orbit coupling which was shown to be weak (see main manuscript). The cRPA is used as implemented in Ref. [11] with a $4 \times 4 \times 4$ k -mesh.

At ambient conditions, we find that the bare, i.e. unscreened, Coulomb interaction $v(\mathbf{r}, \mathbf{r}')$ in the Wannier basis $\chi_{\mathbf{R}\alpha}^{\mathbf{W}}(\mathbf{r})$

$$V_{\mathbf{R}, \mathbf{R}'}^{\alpha\beta\alpha'\beta'} = \frac{e^2}{4\pi\epsilon_0} \times \int d^3r d^3r' \chi_{\mathbf{R}\alpha}^{\mathbf{W}*}(\mathbf{r}) \chi_{\mathbf{R}\beta}^{\mathbf{W}}(\mathbf{r}) \frac{1}{|\mathbf{r} - \mathbf{r}'|} \chi_{\mathbf{R}'\alpha'}^{\mathbf{W}*}(\mathbf{r}') \chi_{\mathbf{R}'\beta'}^{\mathbf{W}}(\mathbf{r}') \quad (1)$$

amounts to $V_{\mathbf{R}, \mathbf{R}}^{\alpha\alpha\alpha\alpha} = 12.0\text{eV}$ for the on-site intra-orbital component of Bi_2CuO_4 . Using the static cRPA polarizability, this interaction is screened down to $U_{\mathbf{R}, \mathbf{R}}^{\alpha\alpha\alpha\alpha} = 2.1\text{eV}$. Figure 5(a) displays the static ($\omega = 0$) values of the density-density components $U_{\mathbf{R}, \mathbf{R}}^{\alpha\alpha\beta\beta}$ within the unit-cell $\mathbf{R} = 0$. In our case orbital-offdiagonal ($\alpha \neq \beta$) components refer to the interaction between $d_{x^2-y^2}$ -derived orbitals of the four equivalent Cu-atoms within the unit-cell. We see that while the decay of the screened interaction with distance is still algebraic (in contrast to a Yukawa-type of potential from e.g., the Thomas-Fermi theory of screening), the nearest neighbor interaction is already reduced to only 0.52eV, i.e. a factor of four smaller than the on-site repulsion. This finding justifies the use of a Hubbard Hamiltonian in which only intra-atomic interactions are retained. Note, however, that the on-site Hubbard U is the energetic price for two electrons to be simultaneously on the same atomic site *relative* to occupying two different sites. It is apparent that any non-local interaction will reduce the *effective* on-site interaction in a model that takes into account only local interactions. Indeed, it can be shown, that to first approximation, the effective on-site interaction is simply given by $U^{eff} = U_{on-site} - U_{nearest-neighbor}$ [13]. Therefore, in our case $U^{eff} = 1.58\text{eV}$. For the one-band/Cu Hubbard model, the gap in the Mott phase will be roughly given by U^{eff} . Given that the experimental (optical) gap has been estimated to be 1.3-1.8eV[14-16], our Coulomb interaction thus seems very reasonable.

Many-body perturbation theory: renormalization of ligand states and exchange self-energies

In the preceding section we computed the screened Coulomb interaction on the basis of the DFT eigenvalues and eigenfunctions and set up the effective Hubbard U to be used in dynamical mean-field (DMFT) calculations for the Cu- $d_{x^2-y^2}$ orbitals.

While this procedure gave a reasonable estimate of the Hubbard U , let us point out possible short-comings of this approach. To this end, we perform electronic structure calculations beyond DFT, using the quasi-particle self-consistent (QS)GW[17] approach. The results are shown Figure 5(b-d) and discussed in the following.

(1) *exchange self-energies of the Cu- $d_{x^2-y^2}$* We first focus on the $d_{x^2-y^2}$ orbitals that are contained in

our low-energy many-body Hamiltonian. The latter is solved using DMFT, which provides a local, on-site, self-energy Σ . As discussed in the main manuscript the system is Mott insulating: The quasiparticle weight $Z = [1 - \partial_\omega \Re \Sigma(\omega)]^{-1}|_{\omega=0}$ vanishes, as the self-energy diverges.

While the perturbative GW approximation is incapable to describe the Mott insulating nature of Bi_2CuO_4 , we nonetheless witness a considerable correlation-induced narrowing of the $\text{Cu-}d_{x^2-y^2}$ dispersion. Within $QSGW$ we find a local quasi-particle weight $Z = 0.29$. From this one would, however, expect a bandwidth-narrowing from $\epsilon^{LDA}(\mathbf{k})$ to $Z \times \epsilon^{LDA}(\mathbf{k})$. Yet, as is apparent in Figure 5(d), the $QSGW$ bandwidth is only about 50% smaller than in DFT. The reason for this is exchange contributions in the GW self-energy that favour the delocalization of charges and hence an *increase* in the bandwidth[18]. This non-local exchange self-energy is included neither in DFT nor DFT+DMFT, and is a major argument for more advanced electronic structure theories, that e.g., combine many-body perturbation theory with DMFT. One example for such a theory is $QSGW$ +DMFT[19].

In our case, where there is only one orbital per copper site, we can easily incorporate the effects of the non-local self-energies into an effective Hamiltonian beyond DFT (for details, see Ref. [19]): The aim is to use the $QSGW$ self-energy to construct an improved—*non-local* self-energy-containing—one-particle Hamiltonian for usage with DMFT, that will add a non-perturbative *local* self-energy. To achieve this we have to assure that local renormalizations are not taken into account twice (“double-counted”). Hence we need to remove all local contributions from the GW self-energy. Here, this simply amounts to rescaling the $QSGW$ bands with the inverse of the local GW quasi-particle weight $1/Z$. The resulting band-structure is shown in Figure 5(d); it has a bandwidth that is *larger* than the DFT one by 27%, as it includes the non-local self-energy that tends to delocalize charge carriers. Again, owing to the one-band nature of our setup, we can alternatively stick to the DFT Hamiltonian and instead *reduce* the value of the Hubbard U^{eff} by 27%, yielding 1.15eV.

(2) *ligand states*. Given the known underestimation of gap values in *sp*-semiconductors and problems of ligand states in e.g., oxides, it stands to reason to question the DFT as viable starting point for screening processes that involve ligand states. So now we focus in our $QSGW$ calculation on bands outside the $\text{Cu-}d_{x^2-y^2}$ subspace. We note that there is a finite (upward) downward shift of (conduction) valence states. As a consequence the $d_{x^2-y^2}$ dispersion gets further isolated and screening effects are likely to become less effective. It can thus be expected that performing the cRPA on top of $QSGW$ will result in an *increased* Hubbard U for the $d_{x^2-y^2}$ orbitals. See also the discussion on CuBi_2O_4 under pres-

sure below. This effect thus competes with the reduction of the Hubbard U discussed in the preceding paragraph. Performing cRPA calculation on top of $QSGW$, we find $U^{on-site} = 2.9\text{eV}$, $U^{nearest-neighbor} = 0.63\text{eV}$. Together with the band-width widening from the preceding section, we thus find an effective interaction $U^{eff} = (U - U_{nn}) \times (1 - 0.27) = (2.9 - 0.6) \times 0.73 = 1.68\text{eV}$ which is almost the same as the LDA result of 1.58eV used in the main text.

Bi_2CuO_4 under pressure: changes in the Hubbard U

Applying pressure to the system will modify both the one-particle dispersion (see Figure 4 in the main text) and the screened Coulomb interaction (Hubbard U). In order to assess whether pressure could drive the system through an insulator-to-metal transition, we here compute the Hubbard U at the experimentally accessible pressure of 50GPa. Quite in general, the impact of pressure onto the Coulomb interaction is two-fold[20, 21]:

(1) *basis functions*. The Wannier basis in which hopping and interaction parameters are expressed is modified. Quite, counter-intuitively, the increased extent of maximally localized Wannier functions under compression *increases* the interaction values[20]. In our case, however, this effect is moderate. Indeed the real-space extend (“spread”) of the Wannier functions increases from 5.42\AA^2 at ambient conditions to 6.52\AA^2 at 50GPa. In fact we find that the bare, i.e., unscreened Coulomb interaction is basically unaffected by pressure with the on-site matrix element changing from $V = 12\text{eV}$ to $V^{50GPa} = 11.7\text{eV}$.

(2) *screening*. In our case the change in the Hubbard U is caused by changes in the particle-hole transitions that screen the bare interaction. These transitions are, within RPA, determined by the one-particle spectrum. As seen in Fig. 4 of the main text, Bi-p orbitals strongly move down in energy and eventually merge into the $d_{x^2-y^2}$ manifold, causing a sizeable increase of the Coulomb interaction screening.

Using this electronic structure of Bi_2CuO_4 under pressure, we find a value of $U = 1.68\text{eV}$ for the on-site matrix element, and an effective U that incorporates the nearest neighbor interaction of $U^{eff} = 1.36\text{eV}$. This value brings us much closer to the interaction-driven insulator-to-metal transition, which happens at $U_c = 1.2\text{eV}$ for the band-structure corresponding to 50GPa. These findings advocate that the double Dirac dispersion can be realized in Bi_2CuO_4 under realistic pressures.

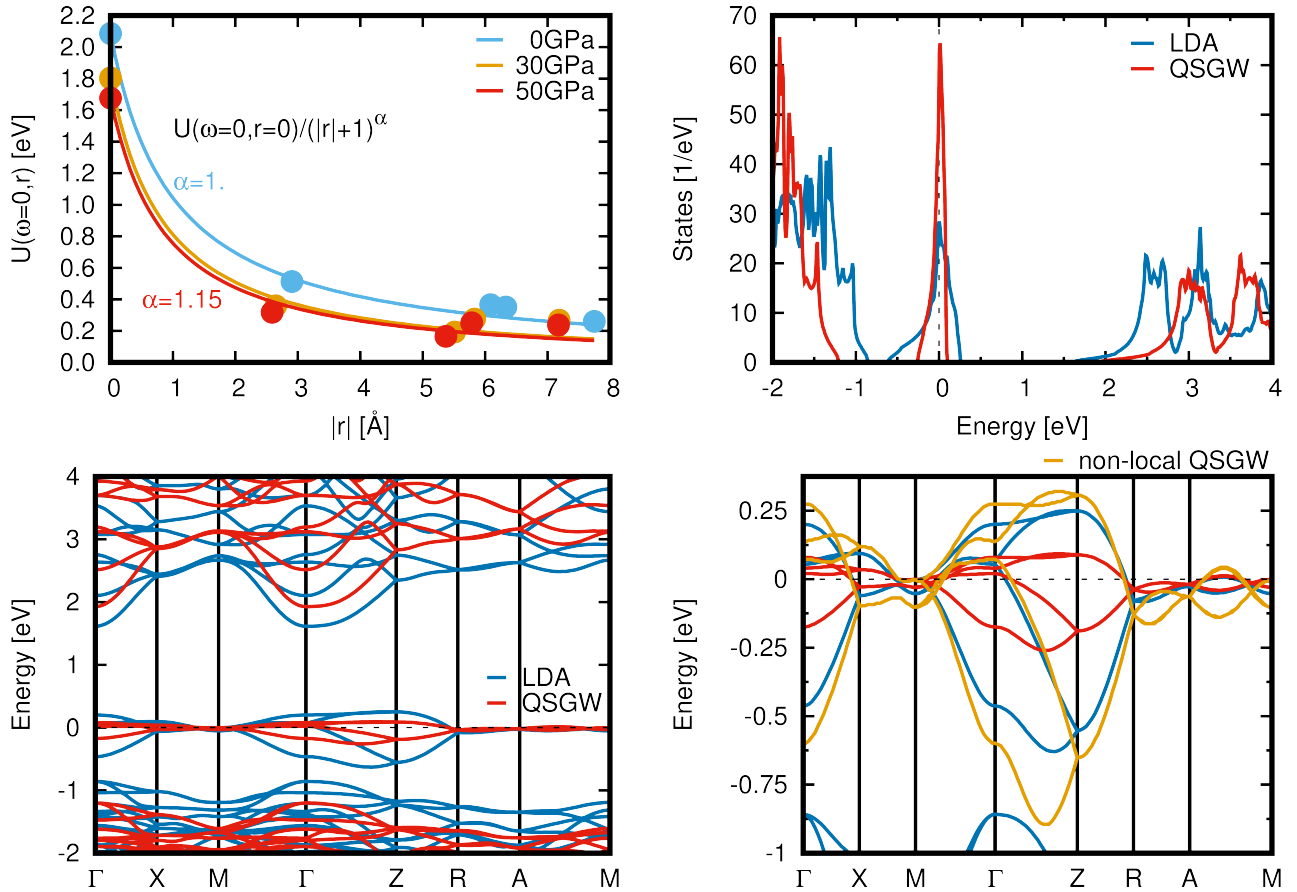


FIG. 5: (a) cRPA results for the static Coulomb repulsion within the CuBi_2O_4 unit-cell. (b-d) QSGW calculations for Bi_2CuO_4 in comparison with LDA results: (b) density of states, (c,d) band-structures along the same k -path as in the main-manuscript. See text for details.

pressure	0GPa	30GPa	50GPa
on-site U	2.1	1.80	1.68
nearest-neighbour U^{nn}	0.51	0.36	0.32
U^{eff}	1.58	1.45	1.36

TABLE III: cRPA values for the interaction in the basis of maximally localized Wannier functions using the LDA band-structure.

Many-body perturbation theory: momentum-dependence of the self-energy

Fig. 6 shows the intra- $d_{x^2-y^2}$ element of the QSGW self-energy in the maximally localized Wannier basis. As apparent from the graph, the self-energies for different k -points (different blue curves) are all parallel to each other, i.e., they differ only by a constant shift. This means that the dynamics of the self-energy is independent of the momentum. Conversely, this implies that the non-locality in the self-energy is purely static: $\Sigma(k, \omega) = \Sigma(k) + \Sigma(\omega)$. This “space-time separation”

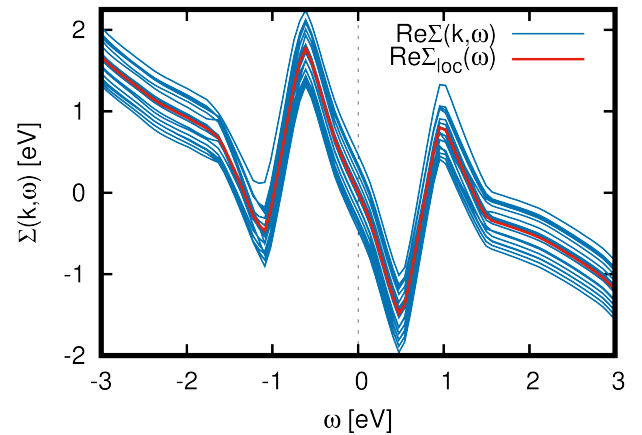


FIG. 6: Real parts of the QSGW intra- $d_{x^2-y^2}$ self-energy for all k -points on a $4 \times 4 \times 4$ Brillouin-zone mesh (blue), and the local (k -summed) element (red). All curves have been arbitrarily shifted by $\text{Re}\Sigma_{loc}(\omega = 0)$.

of the self-energy is in-line with recent findings using the

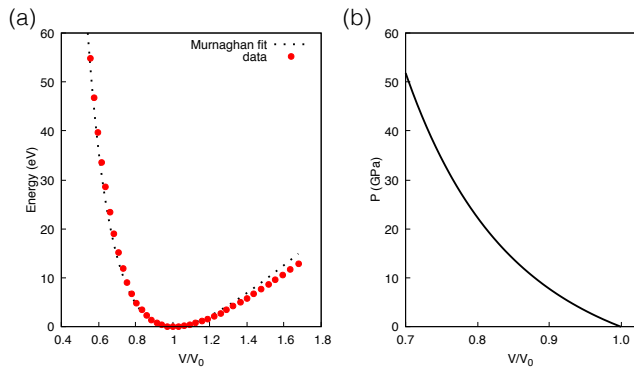


FIG. 7: (a) Energy vs. volume curve and (b) pressure vs. volume curve.

non-perturbative dynamical vertex approximation for the 3D Hubbard model[22].

HYDROSTATIC PRESSURE

To estimate the values of pressure we computed the energy versus volume curve, as shown in Fig. 7(a). Subsequently this curve was fitted using the following Murnaghan equation of state:

$$E(V) = E_0 + \frac{B_0 V}{B'_0} \left[\left(\frac{V_0}{V} \right)^{B'_0} \frac{1}{B'_0 - 1} + 1 \right] - \frac{B_0 V_0}{B'_0 - 1} \quad (2)$$

where E_0 is the energy minimum, V_0 the volume at the minimum, B_0 is the bulk modulus and B'_0 is its derivative with respect to pressure. The obtained parameters were used to produce the $P(V)$ curve

$$P(V) = \frac{B_0}{B'_0} \left[\left(\frac{V_0}{V} \right)^{B'_0} - 1 \right] \quad (3)$$

shown in Fig. 7(b).

U (eV)	J_1	J_2	J_3	J_4
0.0	4.25	5.5	0.07	4.48
0.5	3.5	4.81	0.06	3.72
1.58	2.38	3.75	0.04	2.56
2.1	2.12	3.38	0.03	2.29

TABLE IV: Estimated exchange interactions (in meV) for different values of the U parameter

NÉEL TEMPERATURE

To evaluate the magnetic ordering temperature we map the total energy of different magnetic phases on a

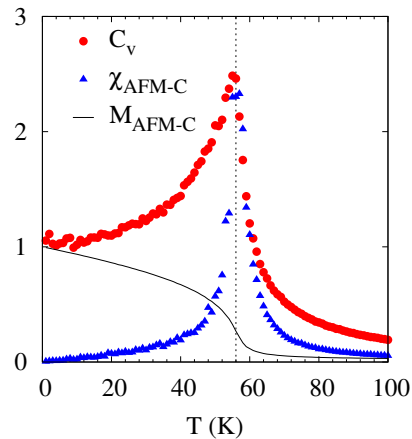


FIG. 8: Specific heat C_V , AFM-C susceptibility χ_{AFM-C} and order parameter M_{AFM-C} as a function of temperature evaluated from exchange interactions at $U = 1.58\text{eV}$.

Heisenberg model

$$H = \frac{1}{2} \sum_{ij} J_{ij} \mathbf{S}_i \mathbf{S}_j. \quad (4)$$

We consider four exchange interactions J_1, J_2, J_3, J_4 , denoting the intra-chain interaction between Cu-1(2) and Cu-4(3) along the c axis (J_1) and three inter-chain interactions between Cu-1 and Cu-2 (J_2), Cu-1 and Cu-3 (J_3) and between Cu-2 and Cu-4 (J_4). Only the four considered magnetic configurations FM, AFM-C, AFM-G and AFM-A can be accommodated in the unit cell, which allows to estimate three independent exchange interactions. Setting the AFM-C energy as the reference, the Heisenberg parameters can be expressed in terms of total energy differences as

$$J_1 = \frac{1}{8S^2} (\Delta E_{FM} - \Delta E_{AFM-A})$$

$$J_2 = \frac{1}{16S^2} \Delta E_{FM} \quad (5)$$

$$J_3 + J_4 = \frac{1}{8S^2} (\Delta E_{FM} + \Delta E_{AFM-G} - \Delta E_{AFM-A})$$

The ratio J_3/J_4 can be then estimated assuming that it is equal to the ratio $(t_{1,3}/t_{4,2})^2$ between the corresponding transfer integrals. The estimated exchange interactions for $S = 1$ and different values of the Coulomb parameter U are given in Table IV.

The Heisenberg model is then used to estimate the Néel temperature from classical Monte Carlo simulations, in order to take spatial non-local fluctuations beyond mean field, the latter being the only one included in single-site DMFT. We used a Metropolis algorithm for $14 \times 14 \times 14$ supercells and 10^7 Monte Carlo steps for averages. The diverging behaviour of the specific heat shown in Fig. 8 as a function of temperature allows one to identify the

critical temperature at which the magnetic ordering sets in. In Fig. 8 we also show the AFM-C order parameter and its associated susceptibility, also displaying a divergence at a critical temperature $T_N \simeq 56$ K.

-
- [1] G. Kresse and J. Furthmüller, Phys. Rev. B **54**, 11169 (1996).
- [2] P. E. Blöchl, Phys. Rev. B **50**, 17953 (1994).
- [3] G. Kresse and D. Joubert, Phys. Rev. B **59**, 1758 (1999).
- [4] J. P. Perdew, K. Burke, and M. Ernzerhof, Phys. Rev. Lett. **77**, 3865 (1996).
- [5] S. Steiner, S. Khmelevskiy, M. Marsmann, and G. Kresse, Phys. Rev. B **93**, 224425 (2016).
- [6] A. A. Mostofi, J. R. Yates, Y.-S. Lee, I. Souza, D. Vanderbilt, and N. Marzari, Comput. Phys. Commun. **178**, 685 (2008).
- [7] A. Georges, G. Kotliar, W. Krauth, and M. J. Rozenberg, Rev. Mod. Phys. **68**, 13 (1996).
- [8] E. Gull, A. J. Millis, A. I. Lichtenstein, A. N. Rubtsov, M. Troyer, and P. Werner, Rev. Mod. Phys. **83**, 349 (2011).
- [9] N. Parragh, A. Toschi, K. Held, and G. Sangiovanni, Phys. Rev. B **86**, 155158 (2012).
- [10] F. Aryasetiawan, M. Imada, A. Georges, G. Kotliar, S. Biermann, and A. I. Lichtenstein, Phys. Rev. B **70**, 195104 (2004).
- [11] T. Miyake and F. Aryasetiawan, Phys. Rev. B **77**, 085122 (2008).
- [12] M. Methfessel, M. van Schilfgaarde, and R. Casali, in Electronic Structure and Physical Properties of Solids: The Uses of the LMTO Method, Lecture Notes in Physics. H. Dreysse, ed. **535**, 114 (2000).
- [13] P. Seth, P. Hansmann, A. van Roekeghem, L. Vaugier, and S. Biermann, ArXiv:1508.07466 (2015).
- [14] A. Abdulkarem, J. Li, A. Aref, L. Ren, E. Elssfah, H. Wang, Y. Ge, and Y. Yu, Materials Research Bulletin **46**, 1443 (2011).
- [15] T. Arai, M. Yanagida, Y. Konishi, Y. Iwasaki, H. Sugihara, and K. Sayama, The Journal of Physical Chemistry C **111**, 7574 (2007).
- [16] N. T. Hahn, V. C. Holmberg, B. A. Korgel, and C. B. Mullins, The Journal of Physical Chemistry C **116**, 6459 (2012).
- [17] S. V. Faleev, M. van Schilfgaarde, and T. Kotani, Phys. Rev. Lett. **93**, 126406 (2004).
- [18] J. M. Tomczak, M. van Schilfgaarde, and G. Kotliar, Phys. Rev. Lett. **109**, 237010 (2012).
- [19] J. M. Tomczak, Journal of Physics: Conference Series **592**, 012055 (2015).
- [20] J. M. Tomczak, T. Miyake, R. Sakuma, and F. Aryasetiawan, Phys. Rev. B **79**, 235133 (2009).
- [21] J. M. Tomczak, T. Miyake, and F. Aryasetiawan, Phys. Rev. B **81**, 115116 (2010).
- [22] T. Schäfer, A. Toschi, and J. M. Tomczak, Phys. Rev. B **91**, 121107(R) (2015).